

# Compressive Wavefront Sensing with Weak Values

Gregory A. Howland,<sup>1,\*</sup> Daniel J. Lum<sup>1</sup>, and John C. Howell<sup>1</sup>

<sup>1</sup>University of Rochester Department of Physics and Astronomy, 500 Wilson Blvd, Rochester, NY 14618, USA

[\\*ghowland@pas.rochester.edu](mailto:ghowland@pas.rochester.edu)

**Abstract:** We demonstrate a wavefront sensor based on the compressive sensing, single-pixel camera. Using a high-resolution spatial light modulator (SLM) as a variable waveplate, we weakly couple an optical field's transverse-position and polarization degrees of freedom. By placing random, binary patterns on the SLM, polarization serves as a meter for directly measuring random projections of the real and imaginary components of the wavefront. Compressive sensing techniques can then recover the wavefront. We acquire high quality,  $256 \times 256$  pixel images of the wavefront from only 10,000 projections. Photon-counting detectors give sub-picowatt sensitivity.

© 2021 Optical Society of America

**OCIS codes:** (110.1758) Computational imaging, (270.0270) Quantum optics, (010.1080) Active or adaptive optics, (120.5050) Phase measurement

---

## References and links

1. F. Roddier, *Adaptive optics in astronomy* (Cambridge university press, 1999).
2. L. N. Thibos and X. Hong, "Clinical applications of the Shack-Hartmann aberrometer," *Optometry & Vision Science* **76**, 817–825 (1999).
3. M. J. Booth, "Adaptive optics in microscopy," *Philosophical Transactions of the Royal Society A: Mathematical, Physical and Engineering Sciences* **365**, 2829–2843 (2007).
4. M. Levoy, "Light fields and computational imaging," *IEEE Computer* **39**, 46–55 (2006).
5. R. Tyson, *Principles of adaptive optics* (CRC Press, 2010).
6. J. S. Lundeen, B. Sutherland, A. Patel, C. Stewart, and C. Bamber, "Direct measurement of the quantum wavefunction," *Nature* **474**, 188–191 (2011).
7. B. C. Platt and R. Shack, "History and principles of Shack-Hartmann wavefront sensing," *Journal of Refractive Surgery* **17**, S573–S577 (2001).
8. R. Lane and M. Tallon, "Wave-front reconstruction using a Shack-Hartmann sensor," *Applied optics* **31**, 6902–6908 (1992).
9. S. Kocsis, B. Braverman, S. Ravets, M. J. Stevens, R. P. Mirin, L. K. Shalm, and A. M. Steinberg, "Observing the average trajectories of single photons in a two-slit interferometer," *Science* **332**, 1170–1173 (2011).
10. J. Z. Salvail, M. Agnew, A. S. Johnson, E. Bolduc, J. Leach, and R. W. Boyd, "Full characterization of polarization states of light via direct measurement," *Nature Photonics* **7**, 316–321 (2013).
11. D. Takhar, J. N. Laska, M. B. Wakin, M. F. Duarte, D. Baron, S. Sarvotham, K. F. Kelly, and R. G. Baraniuk, "A new compressive imaging camera architecture using optical-domain compression," in "Electronic Imaging 2006," (International Society for Optics and Photonics, 2006), pp. 606509–606509.
12. R. G. Baraniuk, "Single-pixel imaging via compressive sampling," *IEEE Signal Processing Magazine* (2008).
13. Y. Aharonov, D. Z. Albert, and L. Vaidman, "How the result of a measurement of a component of the spin of a spin-1/2 particle can turn out to be 100," *Physical review letters* **60**, 1351 (1988).
14. O. Hosten and P. Kwiat, "Observation of the spin hall effect of light via weak measurements," *Science* **319**, 787–790 (2008).
15. P. B. Dixon, D. J. Starling, A. N. Jordan, and J. C. Howell, "Ultrasensitive beam deflection measurement via interferometric weak value amplification," *Physical review letters* **102**, 173601 (2009).

16. A. N. Jordan, J. Martínez-Rincón, and J. C. Howell, "Technical advantages for weak-value amplification: When less is more," *Phys. Rev. X* **4**, 011031 (2014).
17. J. Lundeen and A. Steinberg, "Experimental joint weak measurement on a photon pair as a probe of hardys paradox," *Physical review letters* **102**, 020404 (2009).
18. J. Dressel and A. Jordan, "Significance of the imaginary part of the weak value," *Physical Review A* **85**, 012107 (2012).
19. J. Dressel, M. Malik, F. M. Miatto, A. N. Jordan, and R. W. Boyd, "Understanding quantum weak values: Basics and applications," arXiv preprint arXiv:1305.7154 (2013).
20. D. L. Donoho, "Compressed sensing," *Information Theory, IEEE Transactions on* **52**, 1289–1306 (2006).
21. E. J. Candes, "The restricted isometry property and its implications for compressed sensing," *Comptes Rendus Mathematique* **346**, 589–592 (2008).
22. A. Chambolle and P.-L. Lions, "Image recovery via total variation minimization and related problems," *Numerische Mathematik* **76**, 167–188 (1997).
23. E. J. Candes and T. Tao, "Near-optimal signal recovery from random projections: Universal encoding strategies?" *Information Theory, IEEE Transactions on* **52**, 5406–5425 (2006).
24. M. Lustig, D. Donoho, and J. M. Pauly, "Sparse MRI: The application of compressed sensing for rapid MR imaging," *Magnetic resonance in medicine* **58**, 1182–1195 (2007).
25. J. Bobin, J.-L. Starck, and R. Ottensamer, "Compressed sensing in astronomy," *Selected Topics in Signal Processing, IEEE Journal of* **2**, 718–726 (2008).
26. D. Gross, Y.-K. Liu, S. T. Flammia, S. Becker, and J. Eisert, "Quantum state tomography via compressed sensing," *Physical review letters* **105**, 150401 (2010).
27. G. A. Howland and J. C. Howell, "Efficient high-dimensional entanglement imaging with a compressive-sensing double-pixel camera," *Physical Review X* **3**, 011013 (2013).
28. E. J. Candès and M. B. Wakin, "An introduction to compressive sampling," *Signal Processing Magazine, IEEE* **25**, 21–30 (2008).
29. J. Romberg, "Imaging via compressive sampling [introduction to compressive sampling and recovery via convex programming]," *IEEE Signal Processing Magazine* **25**, 14–20 (2008).
30. C. Li, "Compressive sensing for 3D data processing tasks: applications, models and algorithms," Ph.D. thesis, Rice University (2011).
31. C. Li, W. Yin, and Y. Zhang, "Users guide for TVAL3: TV minimization by augmented lagrangian and alternating direction algorithms," CAAM Report (2009).
32. M. A. Figueiredo, R. D. Nowak, and S. J. Wright, "Gradient projection for sparse reconstruction: Application to compressed sensing and other inverse problems," *Selected Topics in Signal Processing, IEEE Journal of* **1**, 586–597 (2007).
33. G. A. Howland, D. J. Lum, M. R. Ware, and J. C. Howell, "Photon counting compressive depth mapping," *Optics express* **21**, 23822–23837 (2013).
34. J. D. Hunter, "Matplotlib: A 2D graphics environment," *Computing In Science & Engineering* **9**, 90–95 (2007).

## 1. Introduction

High resolution wavefront sensing is extremely desirable for diverse applications in research and industry. Applications include measuring atmospheric distortion for astronomy or communication [1], ophthalmology [2], microscopy [3], light field imaging [4], and adaptive optics [5]. Fundamentally, a wavefront measurement can be equated with measuring the quantum wavefunction [6].

The most common wavefront sensor is the Shack-Hartmann sensor [7, 8], where a high-resolution CCD is placed in the focal plane of a lenslet array. The optical power passing through each lenslet gives a local intensity, while the displacement of each lenslet's focal point on the CCD gives a local phase tilt. Due to the uncertainty principle, Shack-Hartmann sensors are bandwidth-limited; increased spatial resolution comes at the cost of phase precision. A typical Shack-Hartmann sensor might have a spatial resolution of only  $30 \times 30$  lenslets.

Recently, Lundeen et. al. used weak measurement to directly measure the transverse wavefunction of a photonic ensemble [6]. By raster scanning a sliver of waveplate through the field, they weakly couple the field's transverse-position and polarization degrees-of-freedom. After post-selecting on the zero-frequency component of the transverse momentum, the real and imaginary parts of the optical field at the waveplate location are recovered by measuring the final polarization. The measurement is direct; detector values are directly proportional to the real

or imaginary parts of the signal. Similar experiments have used weak measurement to trace the average trajectories of photons in the double slit experiment [9] and to measure the polarization state of a qubit [10].

The technique of Lundeen et. al. is interesting because it has no inherent resolution limitation. However, their measurement process is very inefficient and difficult to scale to high spatial resolution. It requires a slow, physical raster scan of the piece of waveplate through the detection plane. Because the polarization rotation is small, long acquisition times are needed for sufficient signal-to-noise ratio, particularly at low light levels. These limitations make such a system impractical for many applications.

To solve these issues, we present a high resolution wavefront sensor that combines Lundeen et. al.'s technique with the compressive sensing (CS) single-pixel camera [11, 12]. In the usual single-pixel camera, a digital micro-mirror device (DMD) is used in conjunction with a single-element detector to take random, linear projections of an intensity image. Optimization techniques are used to recover the image from many fewer projections than pixels in the image. For a wavefront measurement, we replace the DMD with a twisted-nematic (TN) liquid crystal spatial light modulator (SLM). Each SLM pixel acts as an independent, variable waveplate, allowing us to couple transverse-position and polarization without cumbersome scanning. By placing random, binary patterns on the SLM, we directly measure random projections of the real and imaginary parts of the transverse field at high resolution. The real and imaginary parts of the field are recovered with standard, compressive sensing algorithms.

We efficiently measure optical wavefronts at up to  $256 \times 256$  pixel resolution. Photon-counting detectors provide extreme low light sensitivity, with typical detected optical power around 0.5 pW. Our system is compact and made of affordable, off-the-shelf components. Like the standard single-pixel camera for intensity imaging, our system can be easily adapted to any wavelength where single-element detectors can be manufactured.

## 2. Theory

### 2.1. Weak Measurement

The weak value, originally presented by Aharonov, Albert, and Vaidman as a “new kind of value for a quantum variable” [13], arises from averaging weak measurements on pre- and post-selected systems. Originally a theoretical curiosity, weak measurement has seen resurgent interest as it has turned out to be very useful, particularly for precision measurement [14–16] and investigation of fundamental phenomena, such as Hardy’s paradox [17].

In a weak measurement, a system of interest is investigated by very weakly coupling it to a measuring device. The system is first prepared in an initial state  $|\psi\rangle$ . An observable of interest  $\hat{A}$  is then coupled to an ancillary meter system by a weak interaction or perturbation. Finally, the system is post-selected (projected) into final state  $|f\rangle$ . The weak measurement is read-out by a measuring device for the meter. In the limit of a very weak interaction, the measuring device’s pointer is shifted by the weak value

$$A_w = \frac{\langle f | \hat{A} | \psi \rangle}{\langle f | \psi \rangle}. \quad (1)$$

Note that  $A_w$  can be complex valued. The real part of  $A_w$  is interpreted as a shift in the pointer’s position; the imaginary part of  $A_w$  is interpreted as a shift in the pointer’s momentum [18]. Because the meter’s position and momentum are observables, this enables direct measurement of complex values. For an introduction to experimental weak measurement and weak values, see Refs. [16, 19].

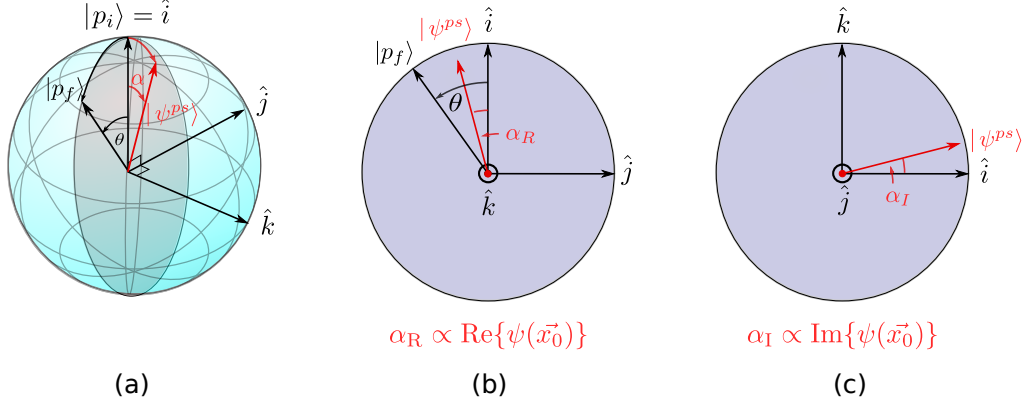


Fig. 1. **Weak Value Wavefront Sensing on the Bloch Sphere:** A state with transverse field  $\psi(\vec{x})$  is initially in polarization  $|p_i\rangle$ . At  $\vec{x} = \vec{x}_0$ , the polarization is rotated by small angle  $\theta$  in the  $(\hat{i}, \hat{j})$  plane to state  $|p_f\rangle$ ; this weakly measures  $\psi(\vec{x}_0)$ . Following a post selection on transverse momentum  $\vec{k} = \vec{k}_0$ , the real and imaginary parts of  $\psi(\vec{x}_0)$  are mapped to a polarization rotation of the post-selected state  $|\psi^{ps}\rangle$ . The real part generates a rotation  $\alpha_R$  in the  $(\hat{i}, \hat{j})$  plane (b) and the imaginary part generates a rotation  $\alpha_I$  in the  $(\hat{k}, \hat{j})$  plane (c). The weak measurement of  $\psi(\vec{x}_0)$  is read-out by measuring  $\langle \hat{\sigma}_j \rangle$  and  $\langle \hat{\sigma}_k \rangle$  respectively.

## 2.2. Wavefront Sensing with Weak Values

We wish to use weak measurement to directly measure an optical field  $\psi(\vec{x})$ , where  $\vec{x} = (x, y)$  are transverse spatial coordinates. In keeping with traditional presentation of weak measurement, we use a quantum formalism where  $\psi(\vec{x})$  is treated as a probability amplitude distribution and polarization is represented on the Bloch sphere. Note that the system can still be understood classically, replacing the wavefunction with the transverse electric field and Bloch sphere with the Poincaré sphere respectively.

Consider a weak measurement of position at  $\vec{x} = \vec{x}_0$  followed by a post-selection of momentum  $\vec{k} = \vec{k}_0$ , where  $\psi(\vec{x})$  and  $\tilde{\psi}(\vec{k})$  are Fourier transform pairs. The corresponding weak value is

$$A_w(\vec{x}_0) = \frac{\langle \vec{k}_0 | \vec{x}_0 \rangle \langle \vec{x}_0 | \psi \rangle}{\langle \vec{k}_0 | \psi \rangle} = \frac{e^{i\vec{k}_0 \cdot \vec{x}_0} \psi(\vec{x}_0)}{\tilde{\psi}(\vec{k}_0)}. \quad (2)$$

$A_w(\vec{x}_0)$  is directly proportional to value of the field at position  $\vec{x} = \vec{x}_0$  up to a linear phase.

To obtain  $A_w(\vec{x}_0)$ , the field at  $\vec{x} = \vec{x}_0$  must be weakly coupled to a meter system. The polarization degree of freedom is a convenient meter because it can be easily manipulated and measured. Let  $\psi(\vec{x})$  be initially polarized in polarization state  $|p_i\rangle$ . The full initial state is

$$|\psi\rangle = \int d\vec{x} \psi(\vec{x}) |\vec{x}\rangle |p_i\rangle. \quad (3)$$

At location  $\vec{x} = \vec{x}_0$ , the polarization is changed from  $|p_i\rangle$  to a nearby polarization  $|p_f\rangle$  (Fig. 1a-b). At location  $\vec{x}_0$ , the state is

$$\psi(\vec{x}_0) |\vec{x}_0\rangle |p_f\rangle = \psi(\vec{x}_0) e^{-i\hat{\sigma}_k \theta/2} |\vec{x}_0\rangle |p_i\rangle, \quad (4)$$

where the transformation from  $|p_i\rangle$  to  $|p_f\rangle$  is expressed as a rotation on the Bloch sphere by angle  $\theta$  about unit vector  $\hat{k}$ . This is visualized on the Bloch sphere in Fig. 1. Unit vectors

$\hat{i}$ ,  $\hat{j}$ , and  $\hat{k}$  form a right handed coordinate system on the Bloch sphere, where  $\hat{i}$  points along  $|p_i\rangle$ ,  $\hat{j}$  is the orthogonal unit vector in the plane defined by  $|p_i\rangle$  and  $|p_f\rangle$ , and  $\hat{k} = \hat{i} \times \hat{j}$  (Fig. 1a-c). These unit vectors have corresponding Pauli operators  $\hat{\sigma}_i$ ,  $\hat{\sigma}_j$ , and  $\hat{\sigma}_k$ . Note that such a coordinate system can be defined for any two polarization states  $|p_i\rangle$  and  $|p_f\rangle$ .

For a weak interaction,  $\theta$  is small. A first order expansion at  $\vec{x}_0$  yields

$$\psi(\vec{x}_0) |\vec{x}_0\rangle |p_f\rangle = \psi(\vec{x}_0) (1 - i\hat{\sigma}_k \theta / 2) |\vec{x}_0\rangle |p_i\rangle. \quad (5)$$

The full state is therefore

$$|\psi\rangle = \int d\vec{x} \psi(\vec{x}) |\vec{x}\rangle |p_i\rangle - \psi(\vec{x}_0) i\hat{\sigma}_k \theta / 2 |\vec{x}_0\rangle |p_i\rangle. \quad (6)$$

Consider post-selection on a single transverse-momentum  $\vec{k} = \vec{k}_0$ . The post-selected state  $|\psi^{ps}\rangle$  no longer has position dependence and is given by

$$|\psi^{ps}\rangle = \langle \vec{k}_0 | \psi \rangle = \tilde{\psi}(\vec{k}_0) |p_i\rangle - e^{i\vec{k}_0 \cdot \vec{x}_0} \psi(\vec{x}_0) i\hat{\sigma}_k \theta / 2 |p_i\rangle, \quad (7)$$

where  $\tilde{\psi}(\vec{k})$  is the Fourier transform of  $\psi(\vec{x})$ .

Factoring out  $\tilde{\psi}(\vec{k}_0)$  and re-exponentiating, we find

$$|\psi^{ps}\rangle = \tilde{\psi}(\vec{k}_0) e^{-ie^{i\vec{k}_0 \cdot \vec{x}_0} \frac{\psi(\vec{x}_0)}{2\tilde{\psi}(\vec{k}_0)} \hat{\sigma}_k \theta} |p_i\rangle = \tilde{\psi}(\vec{k}_0) e^{-iA_w(\vec{x}_0) \hat{\sigma}_k \theta / 2} |p_i\rangle \quad (8)$$

The post-selected polarization state is simply a rotated version of the initial polarization, where the rotation is proportional to  $\psi(\vec{x}_0)$  (Fig. 1a-c). The real part of  $\psi(\vec{x}_0)$  generates a rotation  $\alpha_R$  in the  $\hat{i}, \hat{j}$  plane (Fig. 1b). The imaginary part of  $\psi(\vec{x}_0)$  generates a rotation  $\alpha_I$  in the  $\hat{i}, \hat{k}$  plane (Fig. 1c).

The values are therefore measured by taking expected values of Pauli operators  $\hat{\sigma}_j$  and  $\hat{\sigma}_k$

$$\langle \psi^{ps} | \hat{\sigma}_j | \psi^{ps} \rangle \propto \text{Re}\{\psi(\vec{x}_0)\} \quad (9)$$

$$\langle \psi^{ps} | \hat{\sigma}_k | \psi^{ps} \rangle \propto \text{Im}\{\psi(\vec{x}_0)\}. \quad (10)$$

### 2.3. Random Projections of the Wavefront

Rather than only measuring the wavefunction at a single location  $\psi(\vec{x} = \vec{x}_0)$ , consider instead a weak measurement of an operator  $\hat{f}_i$  which takes a random, binary projection of  $\psi(\vec{x})$ , where  $|f_i\rangle$  is

$$|f_i\rangle = \int d\vec{x} f_i(\vec{x}) |\vec{x}_i\rangle. \quad (11)$$

The filter function  $f_i(\vec{x})$  consists of a pixelized, random binary pattern, where pixels in the pattern take on values of 1 or -1 with equal probability.

The weak measurement of  $\hat{f}_i$ , given initial state  $\psi(\vec{x})$  and post-selected state  $|\vec{k}_0\rangle$ , is therefore

$$A_i = \frac{\langle \vec{k}_0 | f_i \rangle \langle f_i | \psi \rangle}{\langle \vec{k}_0 | \psi \rangle} = \frac{\langle \vec{k}_0 | f_i \rangle Y_i}{\tilde{\psi}(\vec{k}_0)}, \quad (12)$$

where  $Y_i$  is the inner product between  $\psi(\vec{x})$  and  $f_i(\vec{x})$

$$Y_i = \int d\vec{x} f_i(\vec{x}) \psi(\vec{x}). \quad (13)$$

It is convenient to choose  $\vec{k}_0 = (0, 0)$  to discard the linear phase factor  $\langle \vec{k}_0 | f_i \rangle$  in Eq. 12.

To perform the weak measurement, we again couple transverse-position to polarization. Unlike the previous case, all of  $\psi(\vec{x})$  will now receive a small polarization rotation about  $\hat{k}$  of angle  $\theta$  for  $f_i(\vec{x}) = 1$  and  $-\theta$  for  $f_i(\vec{x}) = -1$ ;

Performing an identical derivation to section 2.2, we find a post-selected polarization state

$$|\psi_i^{ps}\rangle = \tilde{\psi}(\vec{k}_0) e^{-i \frac{Y_i}{2\psi(\vec{k}_0)} \hat{\sigma}_k \theta} |p_i\rangle. \quad (14)$$

The effective polarization rotation is now proportional to the projection of  $\psi(\vec{x})$  onto  $f_i(\vec{x})$ ,  $Y_i$ . Again, taking expectation values of  $\hat{\sigma}_j$  and  $\hat{\sigma}_k$  yields the real and imaginary parts of  $Y_i$ ,

$$\langle \psi_i^{ps} | \hat{\sigma}_j | \psi_i^{ps} \rangle \propto Y_i^{\text{Re}} \quad (15)$$

$$\langle \psi_i^{ps} | \hat{\sigma}_k | \psi_i^{ps} \rangle \propto Y_i^{\text{Im}}. \quad (16)$$

Therefore, weak measurement allows us to directly measure random, binary projections of a transverse field  $\psi(\vec{x})$ .

#### 2.4. Compressive Sensing

The random, binary projections of section 2.3 are the type of measurements used in Compressive Sensing [20]. Compressive sensing is a measurement technique that compresses a signal during measurement, rather than after, to dramatically decrease the requisite number of measurements.

In compressive sensing, one seeks to recover a compressible,  $N$ -dimensional signal  $X$  from  $M \ll N$  measurements. The signal  $X$  is linearly sampled by a  $M \times N$  sensing matrix  $F$  to produce an  $M$ -dimensional vector of measurements  $Y$

$$Y = FX + \Phi, \quad (17)$$

where  $\Phi$  is an  $M$ -dimensional noise vector. Measurement vectors (rows of  $F$ ) are often random, binary vectors, so each measurement  $Y_i$  is a random projection of  $X$  [21].

Because  $M \ll N$ , the system of equations in Eq. 17 is under-determined; there are many possible signals consistent with the measurements. CS posits that the correct  $X$  is the one which is sparsest (has the fewest non-zero elements) when compressed. This  $X$  is found by solving a regularized, least squares objective function

$$\min_X \frac{\mu}{2} \|Y - FX\|_2^2 + g(X). \quad (18)$$

The first penalty is small when  $X$  is consistent with  $Y$ . The second penalty,  $g(X)$ , is small when  $X$  is compressible. A common  $g(X)$  for imaging is the Total Variation (TV) of  $X$

$$\text{TV}(X) = \sum_{\text{adj. } i,j} X_i - X_j, \quad (19)$$

where indices  $i$  and  $j$  run over all pairs of adjacent pixels. TV therefore leverages compressibility in the gradient of  $X$ . In this case, Eq. 18 is referred to as Total Variation Minimization [22].

Remarkably, exact recovery of a  $k$ -sparse (only  $k$  significant elements when compressed)  $X$  is possible from only  $M \propto k \log(\frac{N}{k})$  measurements, which can be as low as a few percent of  $N$  [23].

The most well-known example of Compressive Sensing is the single-pixel camera for intensity imaging [12]. A scene of interest  $X$  is imaged onto a digital micro-mirror device (DMD), an array of mirrors which can be individually oriented towards or away from a single-element

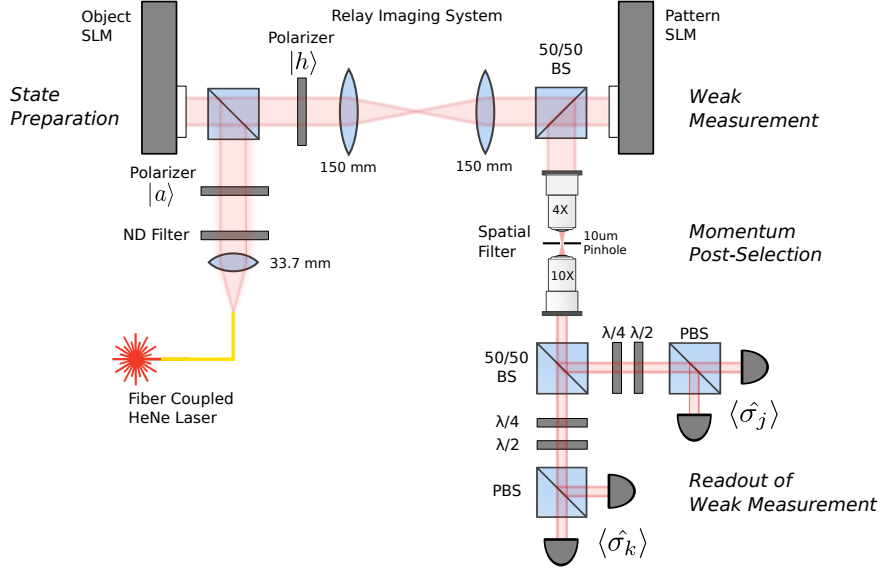


Fig. 2. **Experimental Setup for Wavefront Sensing:** An input field is prepared by illuminating an object SLM with a collimated, attenuated HeNe laser. The input beam is polarized in  $|a\rangle$  to produce a nearly pure phase object with some intensity coupling. A 4F imaging system reproduces the field on a pattern SLM, with a polarizer setting the initial polarization to horizontal ( $|p_i\rangle = |h\rangle$ ). A sequence of  $M$  random, binary patterns are placed on the SLM; pattern pixels with value 1 have their polarization rotated a small amount to  $|p_j\rangle$ . This constitutes a weak measurement of the projection of the input field onto the random pattern. A spatial filter performs the  $\vec{k} = 0$  momentum post-selection. Polarization analyzers take expected values of  $\hat{\sigma}_j$  and  $\hat{\sigma}_k$ , which are proportional to the real and imaginary parts of the projection.

detector. A series of  $M$  random binary patterns are placed on the DMD, each corresponding to a row of sensing matrix  $F$ . The total optical power striking the detector for the  $i^{\text{th}}$  pattern gives the projection of  $X$  onto  $F_i$ , the  $i^{\text{th}}$  measurement  $Y_i$ . Solving Eq. 18 recovers the image.

CS has found many applications including magnetic resonance imaging [24], radio astronomy [25] and quantum entanglement characterization [26, 27]. For a thorough introduction to Compressive Sensing, see Refs. [28, 29].

### 2.5. Compressive Wavefront Sensing

We now have the building blocks to implement a single-pixel, compressive wavefront sensor. We first use weak measurement to take a series of  $M$  random projections of the real and imaginary parts of the wavefront (sec 2.3). We then use compressive sensing optimization algorithms to recover the real and imaginary parts of the field.

The random projections require a device that can perform position-dependent polarization rotations. A twisted-nematic, liquid crystal spatial light modulator (SLM) is capable of this by acting as a variable waveplate. For our SLM, each pixel performs the operation

$$\hat{T}(\vec{x}_0) = |d\rangle\langle d| + \exp(i\Phi(I_{\text{SLM}}(\vec{x}_0))) |a\rangle\langle a|, \quad (20)$$

where  $I_{\text{SLM}}(\vec{x}_0)$  is the SLM intensity at location  $\vec{x}_0$  and  $|d\rangle$  and  $|a\rangle$  refer to diagonal and anti-diagonal polarizations respectively. For a typical 8-bit SLM driven over a VGA video port,  $I_{\text{SLM}}$

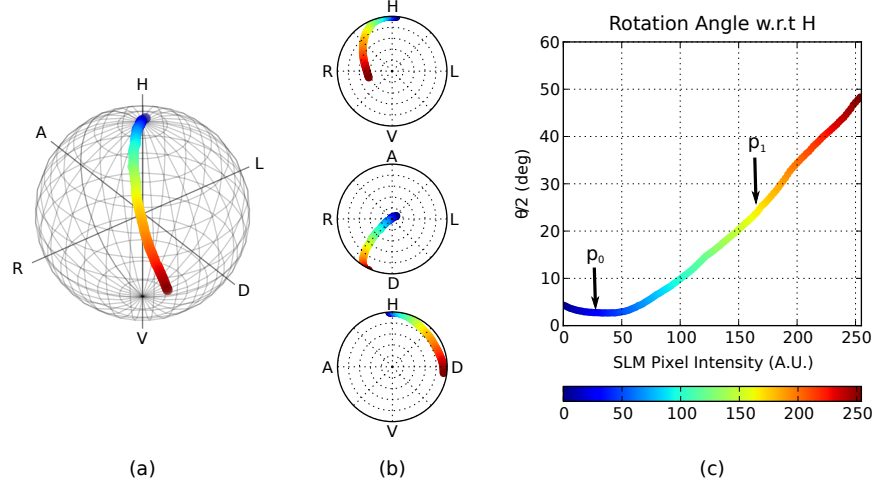


Fig. 3. **SLM Polarization Calibration:** The polarization rotation performed by the SLM on a horizontally polarized input state on the Bloch sphere is given in (a) and (b). (c) gives the angle  $\theta/2$  between the initial horizontal state  $|p_i\rangle$  and output state  $|p_f\rangle$ . Point  $p_0$  corresponds to a minimal rotation less than 1 degree. Point  $p_1$  is the SLM intensity and corresponding angle used for the rotated state  $|p_f\rangle$ , approximately 25 degrees.

takes on integer values of 0 – 255. Because SLM pixels retard  $|a\rangle$  and not  $|d\rangle$ , a non-zero SLM intensity will rotate the polarization of any input state that is not purely  $|a\rangle$  or  $|d\rangle$ .

Let  $N$ -dimensional signal vector  $X = X^{\text{Re}} + iX^{\text{Im}}$  be a one-dimensional reshaping of  $\psi(\vec{x}_0)$ , discretized to the SLM resolution. Let  $F$  be a  $M \times N$ , random, binary sensing matrix whose elements take values 1 or  $-1$  with equal probability. Each row of  $F$  corresponds to a pattern placed on the SLM, where pixels with value 1 rotate the field's polarization by  $\theta$  and pixels with value  $-1$  rotate the field's polarization by  $-\theta$ .

The random projection of  $X$  onto each pattern is weakly measured as in section 2.3 to produce an  $M$ -dimensional measurement vector

$$Y = Y^{\text{Re}} + iY^{\text{Im}} = FX. \quad (21)$$

The real and imaginary parts of  $X$  are recovered by solving Eq. 18.

### 3. Experiment

#### 3.1. Experimental Apparatus

The experimental apparatus is given in Fig. 2. A beam from a fiber-coupled, HeNe laser is collimated by a 33.7 mm focal length lens. A neutral density filter reduces the optical power to the single-photon regime, approximately 0.5 pW. An input field to be measured is prepared with a  $|a\rangle$  oriented polarizer and an object SLM (Cambridge Correlators SDE1024). Because the SLM retards  $|a\rangle$ , an image placed on it will produce a nearly pure phase image with a small amount of amplitude coupling.

A 4F imaging system reproduces the field from the object SLM onto a pattern SLM which is used to perform the weak measurement. A horizontal ( $|h\rangle$ ) polarizer prepares the initial polarization state  $|p_i\rangle$ . A sequence of  $M$  random, binary patterns are placed on the SLM, executing the weak measurement. The patterns consist of randomly-permuted rows of a Hadamard matrix. This dramatically improves reconstruction algorithm speeds as repeated calculations of



$FX$  can be performed by a fast transform [30].

Following the weak measurement, a spatial filter consisting of a 4X microscope objective and a  $10\ \mu\text{m}$  pinhole performs the  $\vec{k} = 0$  post-selection. The Gaussian beam exiting the pinhole is collimated with a 10X objective and directed to a pair of polarization analyzers each consisting of a half-waveplate, quarter-waveplate, and a polarizing beamsplitter. The half- and quarter-waveplates are oriented to measure either  $\langle \hat{\sigma}_j \rangle$  or  $\langle \hat{\sigma}_k \rangle$  for the respective real and imaginary projections. The detectors are large area, photon-counting photomultiplier modules (Horiba TBX-900C).

The difference in the count rate between each polarization analyzer's outputs for each pattern make up  $Y^{\text{Re}}$  and  $Y^{\text{Im}}$ . To solve Eq. 18, we use the TVAL3 solver [31].

### 3.2. SLM Polarization Rotation

A calibration of the SLM polarization rotation as a function of SLM intensity is given in Fig. 3. To calibrate, we illuminate the SLM with a horizontally polarized beam. A uniform intensity was placed on the SLM, and the output polarization was analyzed. The SLM intensity is then scanned through its 8-bit range 0 – 255. Fig. 3a gives the output polarization on the Bloch sphere, with projections into principle planes given in Fig. 3(b). Fig. 3(c) gives the angle  $\theta/2$  between the output polarization and horizontal.

The selected polarization rotation  $\theta/2$  for pixels with value 1 was chosen to be 25 degrees with a corresponding  $I_{\text{SLM}} = 160$ . Because the SLM is not able to simultaneously perform

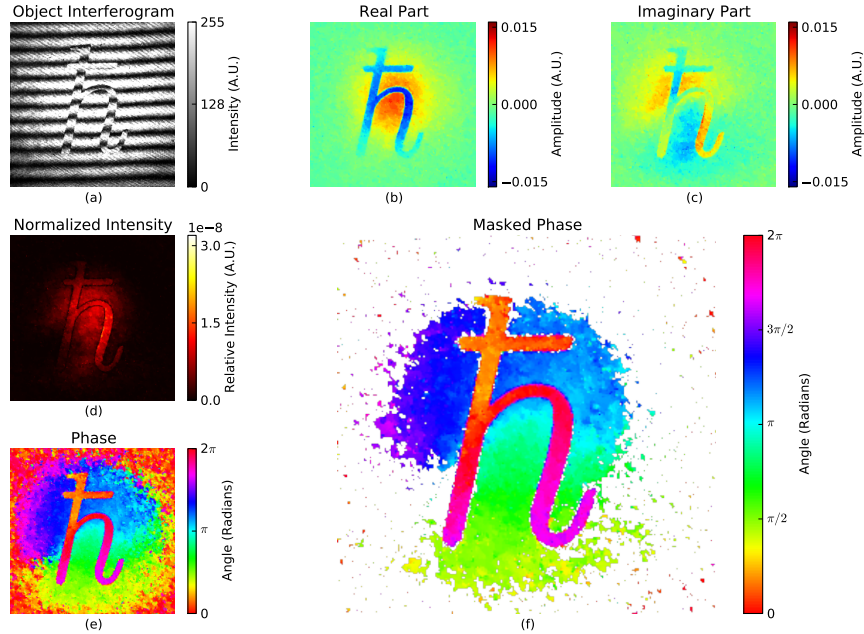


Fig. 4. **256 × 256 pixel  $h$  Character Wavefront:** An interferogram of the object field (a) taken with an 8-bit CCD camera confirms a near-phase-only input wavefront. The CS-reconstructed real and imaginary parts are shown in (b,c), where the wavefront is normalized to unit total intensity. From the real and imaginary parts, we find intensity (d) and phase (e) images. A masked phase image (f) removes all intensities below  $5 \times 10^{-10}$ , where it is not meaningful to assign a phase. Only  $M = 0.15N = 10,000$  random projections are needed for a high quality reconstruction.

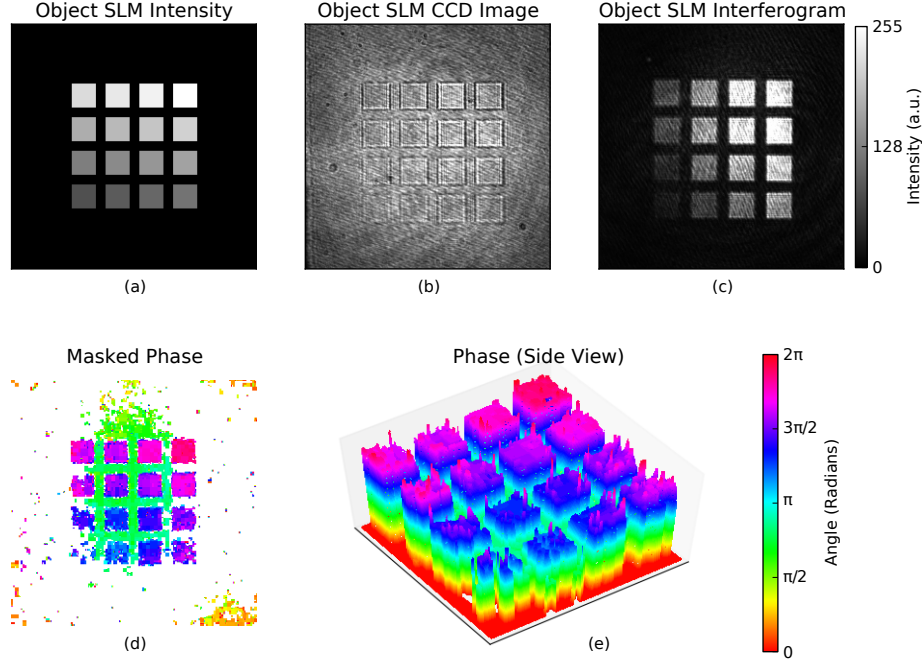


Fig. 5. **Phase Grid Test Pattern:** A 16 square grid of increasing SLM intensity (a) was placed on the object SLM, which converts it to a phase image. A CCD image of the object SLM (b) shows near-uniform intensity, while a dark-port interferogram (c) shows the increasing phase of each square. The phase angle for a  $256 \times 256$  reconstruction is given in (d-e) for  $M = 10000$ . The increasing phase of each square can be seen riding the illuminating beam's Gaussian phase profile.

a  $-\theta/2$  rotation, two measurements must be taken for each SLM pattern  $f_i$ . First, all pixels with value 1 set to  $I_{\text{SLM}} = 160$ , and all pixels with value  $-1$  are set to  $I_{\text{SLM}} = 20$ . The latter experience a polarization rotation less than 1 degree; effectively no rotation. Then, the pattern is inverted; pixels with value  $-1$  are set to  $I_{\text{SLM}} = 160$  and pixels with value 1 are set to  $I_{\text{SLM}} = 20$ . Subtracting the value for the second situation from the first achieves the desired result of a positive  $\theta$  rotation for “1” pixels and a  $-\theta$  rotation for “-1” pixels.

#### 4. Results

The recovered field for a  $256 \times 256$  pixel phase  $\hbar$  character is given in Fig. 4. Fig. 4a shows a camera image of the interference between the object field and reference beam. The image is predominantly a phase-only image with a small amount of amplitude coupling, particularly at the edges of  $\hbar$  character. Fig. 4b-c show the reconstructed real and imaginary parts of field, while Fig. 4d-e give its intensity and phase-angle. The reconstructed field is normalized to have unit total intensity. Fig. 4f gives a masked phase image, where values with negligible intensity below  $5 \times 10^{-10}$  are colored white.

The recovered field has near uniform intensity up to the width of the illumination beam, but a strong variation in phase corresponding to the  $\hbar$  character. Only  $M = .15N = 10000$  random projections were used to recover a high quality image.

Fig. 5 lists the results for a grid of 16 phase squares. Fig. 5(a) is the image placed on the object SLM, where each square increases in intensity from the bottom left to the top right

from  $I_{\text{SLM}} = 30$  to  $I_{\text{SLM}} = 240$ . The SLM converts this image to a phase image. These values were chosen because the polarization rotation appears roughly linear on this range (see Fig. 3). Fig. 5(b) is a CCD image of the object SLM that shows that the object field has near-uniform intensity. Fig. 5(c) gives a dark port interferogram demonstrating the validity of our phase-square reconstruction, where the bottom left square has an almost negligible phase shift with the background while the top right square is nearly  $\pi$  out of phase.

TVAL3 was initially used to solve Eq. 18. However, because of the smoothly varying Gaussian wave-front in the background and additional shot-noise in the measurement process, TVAL3 found a sparse solution in the gradient of the image that did not have a minimized least-squares. Simply stated, TVAL3 found the edges within the image without assigning proper values to them.

As shown in previous work, the solver Gradient Projection for Sparse Reconstruction (GPSR) can be used as a least-squares fitting tool on the largest components of the signal returned by TVAL3 in a Haar wavelet basis [32,33]. A mask was obtained in the pixel basis by neglecting all values less than 4% of the maximum intensity from TVAL3 while least-squares was performed in the wavelet basis with GPSR. The minimized components were then transformed back into the pixel basis and multiplied by our mask to do away with the unwanted artifacts. Fig. 5(d) and 5(e) are the  $256 \times 256$  pixel final results. The reconstructed values accurately reflect the trend set in Fig. 5(c).

## 5. Conclusion

We have demonstrated a wavefront sensor that combines the efficiency and flexibility of compressive sensing with weak measurement. Because our technique directly measures random projections of the real and imaginary parts of a transverse optical field, it is not subject to space-bandwidth product limitations. Compressive sensing makes the technique practical; the transverse field can be acquired from many fewer measurements than pixels ( $M \ll N$ ) with only single-element detectors and without scanning. We anticipate that our technique will be a valuable and useful addition to the field of wavefront sensing and adaptive optics.

## 6. Acknowledgments

The figures in this manuscript were produced in part with Matplotlib [34]. We gratefully acknowledge support from AFOSR grant FA9550-13-1-0019, DARPA DSO InPho grant W911NF-10-1-0404, and ARO grant W911NF-12-1-0263.